Earth Planet. Sci. Lett. 625 (2024) 118495

Contents lists available at ScienceDirect

Earth and Planetary Science Letters

journal homepage: www.elsevier.com/locate/epsl

Multi-scale anisotropy in NE China: Evidence for localized mantle upwelling

Cunrui Han [a,*], James O.S. Hammond [a], Maxim D. Ballmer [b], Wei Wei [c], Mijian Xu [d], Zhouchuan Huang [e], Liangshu Wang [e]

[a] School of Natural Sciences, Birkbeck, University of London, London, UK
[b] Department of Earth Sciences, University College London, London, UK
[c] Key Laboratory of Active Tectonics and Volcano, Institute of Geology, China Earthquake Administration, Beijing, China
[d] Earth Observatory of Singapore, Nanyang Technological University, Singapore, Singapore
[e] School of Earth Sciences and Engineering, Nanjing University, Nanjing, China

ARTICLE INFO

Editor: Dr H Thybo

Keywords:
Intraplate volcanism
Localized upwelling
NE Asia
Asthenospheric flow
Seismic anisotropy

ABSTRACT

It is commonly proposed that the subduction of the Pacific plate has been responsible for widespread Holocene intraplate volcanism across NE China and the Korean Peninsula. Yet, how this process drives volcanism and even if it plays a critical role remains a topic of vigorous debate. In this study, using seismic data from four networks across NE China and northern Democratic People's Republic of Korea (DPRK), we analyze shear wave splitting in converted P to S-waves at the Moho (Pms), S-waves from the subducted slab interface (local S), and SKS phases. The Pms phases show a relatively weak crustal anisotropy (<0.25 s), with fast polarization directions aligned sub-parallel to major tectonic features. For the local S and SKS phases, fast polarization directions show significant lateral variations. We further perform a quantitative inversion to show that the depth of the anisotropy is ~150 km, thus driven by flow within the asthenosphere associated with Pacific subduction. However, the presence of many null SKS splitting phases, together with scattered local S anisotropy across a wide range of incidence angles suggests a localized region of vertical flow directly beneath Changbaishan volcano. Such patterns correspond well to regional upper-mantle seismic velocity structure, and suggest that a localized upwelling with a relatively deep origin drives volcanism in the Changbaishan region. Furthermore, we infer that this mantle upwelling is deflected to the SW beneath Changbaishan and spreads asymmetrically at the base of the lithosphere, possibly because of the long history of volcanism in the region.

1. Introduction

Most volcanic activity is related to plate-boundary processes (e.g., subduction metasomatism or lithospheric extension), yet a number of intraplate volcanoes tend to have more complex and deeper origins (see Ward et al., 2021, for a review). While many intraplate volcanoes can be explained by mantle upwelling from a deep-rooted plume (e.g., Hawaii), others are formed in back-arc settings where subduction is often thought to drive volcanism. An archetypal example of this is NE China, where a unique trench-arc-back-arc system has been formed due to the subduction of the western Pacific plate beneath the Eurasian plate (Fig. 1). Several Holocene intraplate volcanoes (i.e., Changbaishan; also known as Paektu/Baekdu in Korean, Ulleung-do, Longgang, Jingpohu and Wudalianchi) overlie the Pacific slab that stagnates in the mantle transition zone (MTZ), however, the origin of these volcanoes remains widely debated.

As part of the Central Asian Orogenic Belt, NE China has undergone multiple episodes of Paleozoic collision, Mesozoic-Cenozoic extension as well as the Pliocene contraction, all shaping the current topography (Liu et al., 2001; Tian et al., 1992; Wilde, 2015). Several major boundary faults divide the study region into three main blocks: the Great Xing'an range, Songliao basin and Jiamusi block (Fig. 1). The spatial distribution of Holocene volcanism is closely associated with boundary faults. Apart from the relatively isolated Wudalianchi volcano, the Longgang, Jingpohu and Changbaishan align NE-SW, which is consistent with the strike of the pre-existing Yitong-Yilan fault and Dunhua-Mishan fault. Changbaishan is located at the intersection of Dunhua-Mishan fault and several NW-SE trending local faults that extend into the Democratic

* Corresponding author.
E-mail address: c.han@bbk.ac.uk (C. Han).

https://doi.org/10.1016/j.epsl.2023.118495
Received 27 June 2023; Received in revised form 2 November 2023; Accepted 10 November 2023
Available online 23 November 2023

People's Republic of Korea (DPRK, the formal name for North Korea; Fig. S1). Among these volcanoes, Changbaishan is the most active, with the 946 CE eruption identified as one of the largest historic eruptions (e.g., Oppenheimer et al., 2017). From 2002 to 2005, volcanic unrest indicated the movement of magma at depth (Xu et al., 2012), showing the potential for this volcano to erupt in the future.

Seismic imaging and geodynamic studies have proposed various underlying mechanisms, including slab dehydration in the so-called 'big mantle wedge' (BMW) above the stagnant Pacific slab (e.g., Zhao et al., 2012), upwelling of a hydrous transition zone caused by subduction return flow (Yang and Faccenda, 2020), localized return flow through a slab gap in the Pacific slab (Kim et al., 2021; Tang et al., 2014; Tao et al., 2018), self-buoyant hydrous upwellings (Long et al., 2019), or upwelling caused by lithospheric delamination (Wei et al., 2019). Geochemical studies further point to a deeper source for these Holocene intraplate volcanoes, as the trace element composition of magmas are similar to OIB (Ward et al., 2021), tapping EM1/LoMu reservoirs that are likely associated with the MTZ.

On the other hand, the inherent lithospheric structure seems to play an important role in the interaction with the upwelling magma. Changbaishan, Longgang and Jingpohu are sodic volcanoes with a mixed asthenospheric source, while Wudalianchi is more potassic showing contamination by the subcontinental lithospheric mantle (Wang et al., 2017). Significant differences have been revealed in the morphology and physical properties of the crust and lithosphere. Overall, the crustal and lithospheric thickness increases gradually from SE to NW across the Songliao basin (He et al., 2022; Tao et al., 2014), while the Jiamusi block is stable with a relatively thick lithosphere (Zhang et al., 2014). Seismic imaging clearly shows low-velocity anomalies in the uppermost mantle beneath Changbaishan, Jingpohu and Longgang, as well as a locally thickened lithosphere (Fan et al., 2021; Zhang et al., 2022) and crust (e.g., Hammond et al., 2020).

Seismic anisotropy, being sensitive to the alignment of olivine in the presence of mantle flow, is a useful tool to link these snapshots of mantle velocity structure to dynamic processes, as the rock fabric in the upper mantle records the vigor and direction of mantle flow over millions of years. Previous studies have emphasized widespread horizontal mantle flow (i.e., trench normal) associated with the geometry of the Pacific plate and slab rollback (e.g., Fan et al., 2020; Li et al., 2017), but their constraints on the vertical flow in the mantle, especially beneath Changbaishan, are still insufficient. A unique opportunity to overcome this limitation, and therefore better constrain mantle flow beneath these volcanoes, comes from recent collection of seismic data in NE China. Permanent stations deployed by the Chinese earthquake administration (CEA) have been recording data for more than ten years, enhanced by a number of temporary deployments. During this time, a significant number of deep earthquakes have been recorded that are suitable for shear wave splitting analysis. This provides a rare opportunity to constrain the spatial distribution of anisotropic properties by analysis of multiple seismic phases.

In this study, we analyze the splitting characteristics of the local S, Pms, and SKS phases, and perform a quantitative inversion to determine the depth of origin of the measured anisotropy. Our new findings indicate that crustal anisotropy is highly correlated with regional tectonics,

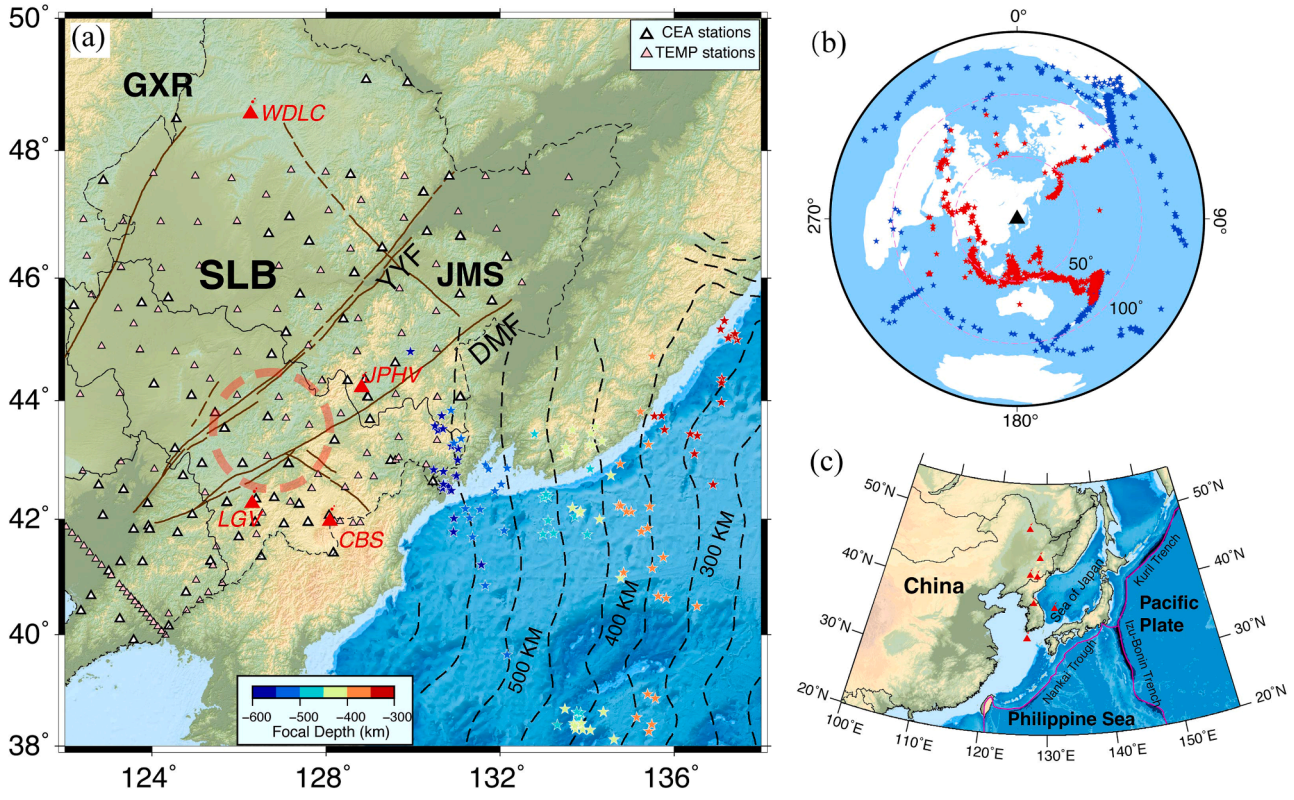

Fig. 1. Tectonic setting of NE Asia with station and earthquake distribution. (a) The tectonic blocks in the study area include the GXR—Great Xing'an range, SLB—Songliao basin and JMS—Jiamusi block. The boundary faults are represented by brown solid line, including the YYF—Yilan-Yitong fault and DMF—Dunhua-Mishan fault. Station distribution is represented by triangles (permanent stations in white and temporary stations in pink). Holocene volcanoes include CBS—Changbaishan, LGV—Longgang, WDLC—Wudalianchi and JPHV—Jingpohu. The stars denote the distribution of local earthquakes, with the color representing the focal depth. Dashed lines show slab contours based on seismicity from Hayes (2018). Tomography shows that most of the study region is underlain by a stagnant slab in the transition zone (e.g., Zhao et al., 2012), but the red dashed circle represents the location of a potential slab gap in model of Tao et al. (2018) (b) Distribution of teleseismic earthquakes. Red stars represent earthquakes used for receiver function calculation and blue ones represent events used for SKS splitting calculation. (c) Tectonic setting and Holocene volcanoes in NE Asia. (For interpretation of the references to color in this figure legend, the reader is referred to the web version of this article.)

while anisotropy in the mantle provides evidence for localized upwelling beneath Changbaishan, consistent with seismic tomography models, elucidating the most likely source of recent volcanism in NE China.

2. Data and methods

2.1. Data

The seismic waveforms used in this study are recorded by 4 networks (Fig. 1; Table S1), including 82 permanent stations of the CEA network from January 2009 to September 2021, 165 NECESSArray stations from January 2007 to December 2011 (Ai and He, 2007; Grand and Ni, 2009), 6 temporary stations of the MPGG array deployed in the DPRK from January 2013 to December 2015 (Mount Paektu Research Centre, 2013) and 17 stations of the Dongbei Broadband Network from January 2004 to December 2010 (Chun and Richards, 2004).

We measure anisotropy in three separate seismic phases; Pms, SKS and local S. For the Pms phase, we retained earthquakes with magnitude $\geq$5.5 and epicentral distances ranging from 30° to 90°, while for the SKS phases, we use earthquakes with magnitude $\geq$6.0 and epicentral distances ranging from 85° to 140°. For the local earthquakes in the study region, we collected earthquakes with magnitude $\geq$4.0 and focal depth $\geq$300 km from the U.S. Geological Survey (USGS) catalog (Fig. 1). We check to make sure all local earthquakes have an incidence angle of $<$35° to ensure clear S-wave time window and avoid contamination from surface effects. The mean shift and linear trend are all removed routinely as well. Chen et al. (2017) showed that compared to temporary seismic arrays in the study region, CEA permanent stations may have problems with misorientation. In order to avoid this influence on measuring the anisotropy, we also rotate the horizontal components for the CEA permanent stations by using the P-wave polarization correction method (Niu and Li, 2011) before further analysis. The inclusion of long-term observations of the permanent stations provides considerable numbers of events (especially for the local deep earthquakes) and azimuthal coverage (e.g., Bi et al., 2020), while the dense temporary stations can improve the spatial constraints.

2.2. Crustal anisotropy

The Pms phase generated by a conversion from P to S-waves at the Moho can be used to constrain the accumulated anisotropy of the crust. In this study, we used the multi-channel method developed by Liu and Niu (2012) to measure the crustal anisotropy from the receiver functions. Following the procedure in Xu et al. (2020), we removed the mean shift and linear trend in the waveforms and filtered them with a fourth-order Butterworth filter in the band of 0.05–2 Hz, and then calculated the P-wave receiver functions with a time domain iterative deconvolution with a maximum iteration of 400 or a misfit reduction of less than 0.001 between the last two iterations. A simple and weakly anisotropic crust will lead to a periodic variation of both the radial and transverse receiver functions with back azimuth, which, assuming a horizontal symmetry axis in a relatively simple crust (Park et al., 2023), can be used to constrain the anisotropy parameters. We search for the pair of φ and δt that best satisfies the following conditions: (1) maximize the peak energy of the stacked R receiver function after a cosine moveout correction in the Ps arrival time; (2) maximize the cross-correlation of the radial receiver functions after a full correction of crustal anisotropy; (3) minimize the total energy of transverse receiver functions stacked after removal of crustal anisotropy. These three individual objective functions are weighted (0.4, 0.4, 0.3 in this study) and combined in a joint misfit function. More details on the method can be found in Liu and Niu (2012). To avoid uncertainty, we only keep the results where the three independent functions are consistent, that is, the splitting parameters can be independently constrained through each of the three conditions (Fig. 2).

2.3. Shear wave splitting

The shear wave splitting method has been a powerful tool for measuring anisotropy in the Earth's interior for the past 30 years (e.g., Vinnik et al., 1984). In this study, we used the minimum transverse energy method for SKS splitting analysis and the minimization of the second eigenvalue method for local S wave splitting analysis (Silver and Chan, 1991) to obtain the splitting parameters (φ and δt). Both methods adopt a grid search algorithm to find the splitting parameters by rotating and time-shifting the R-T components. The ranges in grid search for φ and δt are $-90°$ to 90° with an increment of 1° and 0 to 4 s with an increment of 0.05 s, respectively. The uncertainties are estimated by the 95 % confidence region of the F test with the updated calculation of the degrees of freedom (Walsh et al., 2013). Moreover, we used the cluster analysis method proposed by Teanby et al. (2004) to increase the reliability of the results (for more details please see Bi et al., 2020; Figs. 3 and S2). For the SKS splitting, all waveforms are filtered with a band-pass filter between 0.05 and 0.4 Hz. For the local S splitting, we filter between 0.1 and 0.6 Hz. The SKS and local S splitting were analyzed by using a Python toolkit (Bi et al., 2020) developed over the SHEBA software (Wüstefeld et al., 2010).

We classify different shear wave splitting results as "good", "fair", "poor" and "null". For the results of "good" and "fair", the elliptical particle motion is corrected to be linear, and the tangential energy is close to zero. The optimal solution converges in the error surface, and are stable for different picked time windows (Figs. 3(a) and S2). For the null results, the particle motion of the original waveform is always linear with minimal tangential energy. The error surface often presents a symmetrical pattern, and the optimal solution varies in a wide range (Fig. 3(b)).

2.4. Estimate of the depth of anisotropy

Contributions to shear wave splitting measurements are defined by the width of the Fresnel zone through the anisotropic region (e.g., Salimbeni et al., 2008). This means that, when nearby sites display different splitting signals for the same phase, the cause of the difference has to lie in a region where the ray paths of the corresponding waves diverge enough for the Fresnel zones to separate (Levin et al., 2018). Based on the simplified spatial coherency method presented by Liu and Gao (2011), we quantitatively invert for the source depth of the measured anisotropy (i.e., local S and SKS phases). We back-project all measurements to the pierce points at different depths along the ray paths. The optimal anisotropy depth is searched in the 0–300 km range to reach the highest spatial coherency of the observed splitting parameters. The incremental interval for the assumed depths is 5 km. In brief, for each depth, the study area is divided into N overlapping cells with an area of $dx * dx$ square-degrees. The variation factors at this depth, $F_{\delta t}$ for δt and F_{φ} for φ, are average values of standard deviation for each cell. They are calculated using the following equations (Liu and Gao, 2011):

$$F_{\delta t} = \frac{1}{N}\sum_{i=1}^{N}\sqrt{\frac{1}{M_i - 1}\sum_{j=1}^{M_i}\left(\delta t_{ij} - \overline{\delta t_i}\right)^2} \tag{1}$$

and

$$F_{\phi} = \frac{1}{N}\sum_{i=1}^{N}\sqrt{-\frac{1}{2}\ln(R_i)} \tag{2}$$

where

$$R_i^2 = \left[\frac{1}{M_i}\sum_{j=1}^{M_i}\cos\left(2\phi_{ij}\right)\right]^2 + \left[\frac{1}{M_i}\sum_{j=1}^{M_i}\sin\left(2\phi_{ij}\right)\right]^2 \tag{3}$$

N is the number of blocks, M_i is the number of measurements for the ith block, ϕ_{ij} and δt_{ij} are the jth fast polarization direction (FPD) and delay time measurement in the ith block. $\overline{\delta t_i}$ is the average over all the

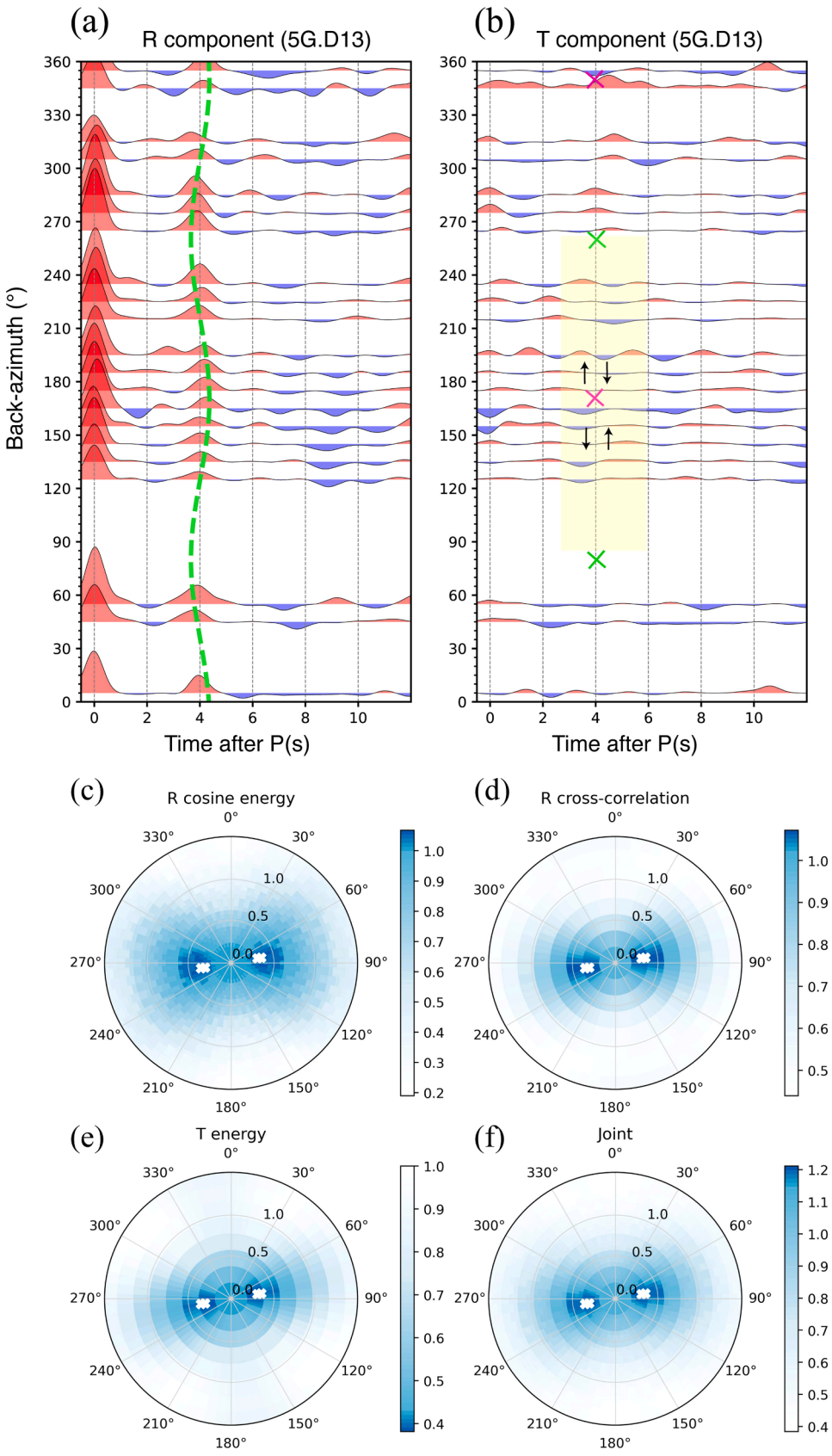

(caption on next page)

Fig. 2. Example of crustal anisotropy inversion for station 5G.D13. (a,b) Radial and transverse receiver functions. The green dashed line in the radial receiver function highlights the theoretical arrival time of Pms arrival time assuming crustal anisotropy of 80° and 0.3 s. The green and magenta crosses in the transverse receiver functions highlight the back-azimuth of the polarity reversal. The yellow shading and black arrows represent the polarity reversal in the observed receiver function. (c-f) The misfit functions, including (c) the energy of the stacked corrected radial receiver function, (d) the cross-correlation of the corrected radial receiver functions, (e) the total energy of corrected transverse receiver functions, (f) the joint misfit function inversion. (For interpretation of the references to color in this figure legend, the reader is referred to the web version of this article.)

measurements in block *i*. The overall variation factor, *Fv*, is computed as a dimensionless weighted average of F_{φ} and $F_{\delta t}$:

$$F_v = w_{\phi}F_{\phi} + w_{\delta t}F_{\delta t} \quad (4)$$

where w_{ϕ} and $w_{\delta t}$ are the weighting factor for the ϕ and δt measurements (0.7 and 0.3 in this study, respectively). Consequently, lower *Fv* implies higher coherence of the splitting parameters, predicting the most probable source depth of the measured anisotropy (Liu and Gao, 2011).

3. Results

For the crustal anisotropy, the thick sediments of the Songliao basin generate strong reverberations, which tend to dominate the receiver function masking any Pms signals. Therefore, in this study we ignore the inversion for stations in the basin interior and estimate crustal anisotropy measurements at 87 stations (Fig. 4(a); Table S2). To the east of Songliao basin, most of the FPDs are ENE-WSW trending, parallel to the strikes of Dunhua-Mishan fault and Yitong-Yilan fault. In addition, some NW-SE trending FPDs are measured, which are parallel to local faults (Fig. S1). Most of the splitting times remain low, with the average less than 0.25 s.

We also obtain 321 "good", 244 "fair" and 30 "null" results for local S splitting and 133 "good", 197 "fair", and 110 "null" results for SKS splitting (Fig. 4(b) and (c); Table S3). We stack the error surface and obtain the average splitting parameters for each station (Fig. S3). Overall, the FPDs from local S splitting around Changbaishan, Longgang and Jingpohu show a circular pattern (i.e., from NW-SW trending in Changbaishan and Longgang to E-W trending in Jingpohu) while the regional average δt is 0.65 s. In contrast, the FPDs from SKS splitting show strong lateral variations in different regions, that is, NNW-SSE trending in Great Xing'an range and Jiamusi, E-W trending in Songliao basin interior and NW-SE trending to the east of Dunhua-Mishan fault. It is worth noting that many null results are detected, particularly in the region surrounded by Changbaishan and Longgang despite these events having a wide range of back-azimuths. Support for these strong lateral differences in splitting can be seen in SKS waveforms for a single event observed throughout the NE China, which shows minimal energy on the transverse component for those stations measuring "null" compared to those stations where splitting is observed (Fig. S4). Fig. 4 (d) shows the combination of the three splitting measurements in three specific regions. Overall, the splitting times of Pms are much smaller than those of local S and SKS throughout the study region. Beneath Changbaishan, SKS phases with low incidence angles show mostly "null" results, while local S measurements, with higher incidence angles, show NW-SE oriented FPDs. For the location on the periphery of Jingpohu volcano, local S and SKS measurements are very consistent. The absence of azimuthal variations in the apparent splitting parameter in these regions also precludes the presence of multi-layered anisotropy and indicates that crustal or lithospheric anisotropy has minimal effect on the apparent splitting parameter. One exception is in the interior of the Jiamusi block, where local S and SKS measurements display significant lateral differences, which may be indicative of multiple anisotropic sources underneath, possibly in the lithosphere or close to the subducted slab (e.g., Bi et al., 2020; Liu et al., 2008).

While stacked splitting parameters are useful for SKS splitting, where raypaths in the uppermost mantle are sub-vertical thus travel similar paths regardless of back-azimuth, such stacking is less useful for local S-waves as they have a wider range of incidence angles (although all $<35°$), thus sampling different parts of the mantle at depth. Using the IASP91 velocity model, we project local S and SKS measurements to the pierce points at different depths (Figs. 5 and S5). When projected to depths of 150 km, the splitting parameters (i.e., FPDs and delay times) from local S and SKS appear similar. As the depth increases, the measurements at the same location tend to be more scattered. Spatial coherency analysis suggests that the optimal depth for the anisotropic source lies approximately between 125 km and 175 km (Fig. 6). Different *dx* test values from 0.16° to 0.28° with an interval of 0.04° were utilized to generate the *Fv* curves. The results for the 4 grid sizes showed the same trend, and we finally chose the smoother results to analyze with a grid size of 0.28°. At this depth, all measurements in three specific regions are more consistent (Fig. 6(b)). We also calculate the coherence of each grid to examine the lateral variations across the study area at different depths (Fig. S6). This analysis shows that most of the measurements of local S and SKS are consistent across the study area (that is, with lower *Fv*), except the region around Changbaishan and Longgang where the consistency is relatively poor. This signals the possibility of more complex anisotropic features (e.g., multi-layered or non-horizontal anisotropic alignments) beneath the region (see Section 4.2 for further discussion).

4. Discussions

4.1. Lithospheric deformation

Anisotropy in the Earth's interior may have different causes at depth. In general, anisotropy in the upper crust is caused by the alignments of fractures, with the fast direction parallel to the strike of active faults or plate boundaries (e.g., Crampin, 1984; Han et al., 2020), while the anisotropy in mid-lower crust and mantle lithosphere results from the lattice-preferred orientations (LPO) of intrinsically anisotropic minerals (e.g., mica, olivine; Mainprice, 2007), with the FPD typically parallel to the maximum strain or shear direction. In addition, potential fine-scale layering, horizontal foliation, and aligned magmatic dykes or partial melt can also contribute to crustal anisotropy and exhibit significant azimuthal variations in receiver functions (e.g., Bianchi et al., 2023; Hammond, 2014; Paulssen, 2004). In this paper, we only constrain a uniform horizontal-axis anisotropy. More modeling is required to investigate other more complex models such as depth variation of the anisotropic properties (Park et al., 2023). Most of the crustal FPDs are consistent with the strikes of regional fault zones, indicating that the measured anisotropy in Pms phases is mainly caused by the mineral or fracture alignment due to shearing along the fault (Fan et al., 2020). Most of the splitting times remain low (less than 0.25 s), while the average crustal thickness is about 30 km (Tao et al., 2014), representing an average 1.5 % anisotropy for the crust.

Furthermore, Zhang et al. (2022) predicted the thermally defined depth of the lithosphere-asthenosphere boundary (LAB) to be ~85 km based on the surface heat flow and S-wave velocity structure for the entire lithosphere in NE China, a result supported by recent S-wave receiver functions (He et al., 2022) across the southern half of our study area. In contrast, Zhang et al. (2014) revealed thicker lithosphere in the northern half (i.e., 100–120 km beneath the Songliao basin but 120–140 km beneath southern Jiamusi). This finding suggests that the mantle lithosphere beneath the volcanic regions is relatively thin. Deep seismic reflections indicate that both the Yitong-Yilan fault and Dunhua-Mishan fault extend through the entire crust into the upper mantle (Xu et al.,

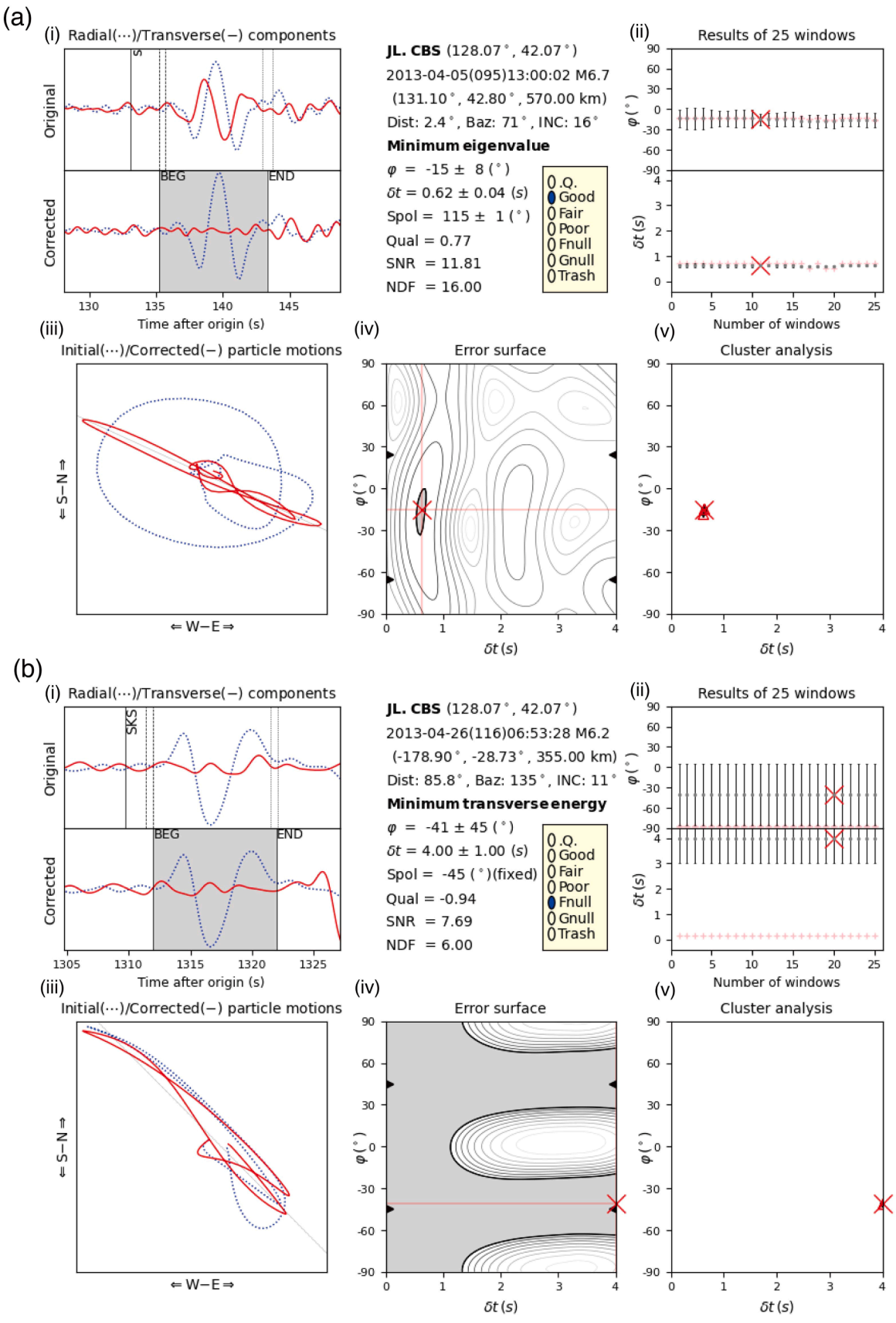

(caption on next page)

Fig. 3. Examples of two "Good" splitting measurement of local S (a) and SKS (b) for station CBS. (i) Radial (Q, blue) and transverse (T, red) components before and after correction. The shaded area in the corrected box shows the picked time window on which the optimal splitting result is measured. (ii) Measurements of φ and δ_t obtained from 25 different time windows are plotted in the top-right against the window number. The gray dots denote individual measurements with the minimization of the second eigenvalue or Minimum transverse energy method. The measurements using the rotation-correlation method (Bowman and Ando, 1987) are also plotted as pink crosses but only for reference. The short bars indicate the corresponding uncertainties (95 % confidence region). The solution that is selected using cluster analysis is marked with the red cross. (iii) Particle motion before (blue) and after (red) splitting correction. (iv) Map of minimum value of the error surface. (v) Cluster analysis of the 25 pairs of splitting parameters. Note that an example of "null" result is shown in (b), for a station close to Changbaishan. (For interpretation of the references to color in this figure legend, the reader is referred to the web version of this article.)

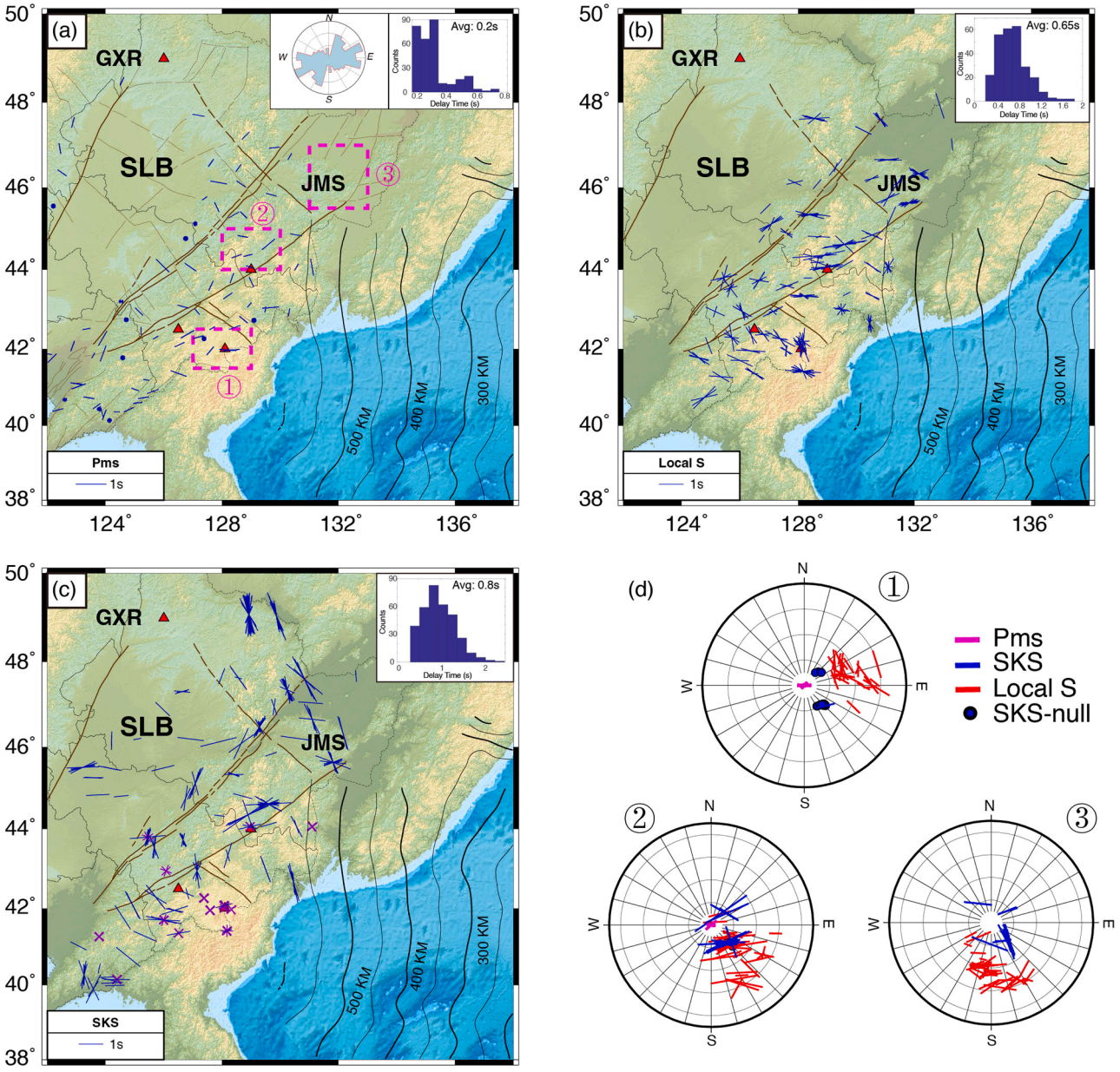

Fig. 4. Splitting measurements for Pms (a), local S (b) and SKS (c), respectively. The direction of the short blue bar indicates the FPD while its length indicates the splitting time. The inset on the top right shows the histogram of the splitting times. The mean values of the measurements for Pms, local S and SKS phases are 0.2 s, 0.65 s, 0.8 s, respectively. The short violet bars in (c) indicate the back-azimuth of the "null" measurement and its orthogonal direction. (d) Stereograms for the splitting parameters of the three seismic phases at three specific sites shown in (a). (For interpretation of the references to color in this figure legend, the reader is referred to the web version of this article.)

2017). Therefore, the mantle lithosphere may have a similar deformation history and anisotropy pattern as the crust (i.e., the FPD is constant and the splitting time increases linearly with the thickness). However, both the accumulated splitting time (less than 0.7 s, assuming a lithospheric thickness of 80 km) and fast direction deviate from the observations of local S and SKS phases, suggesting a deeper, asthenospheric origin of anisotropy is present.

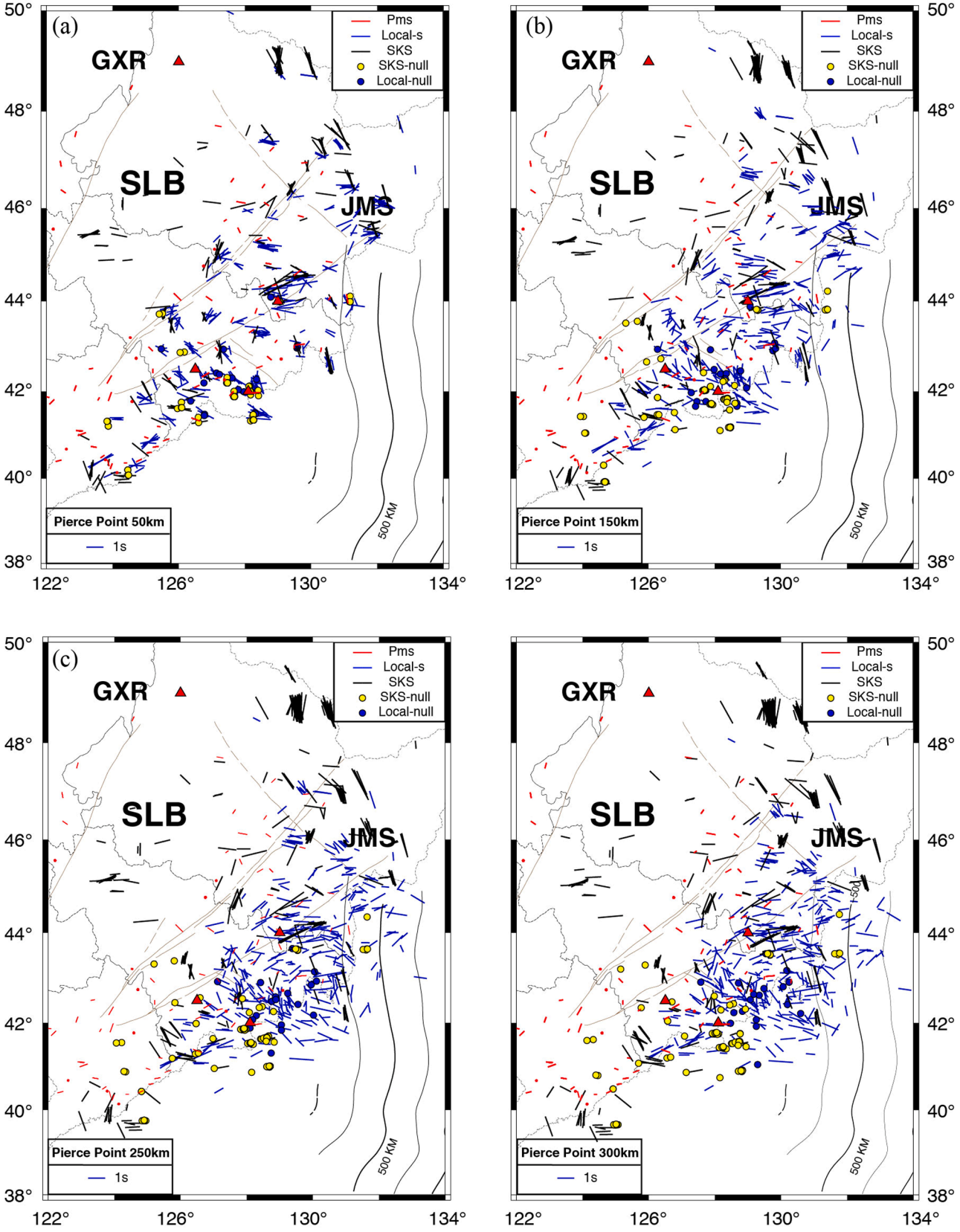

Fig. 5. (a–d) Plots of all splitting measurements projected to different pierce points (50 km, 150 km, 250 km, 300 km, respectively).

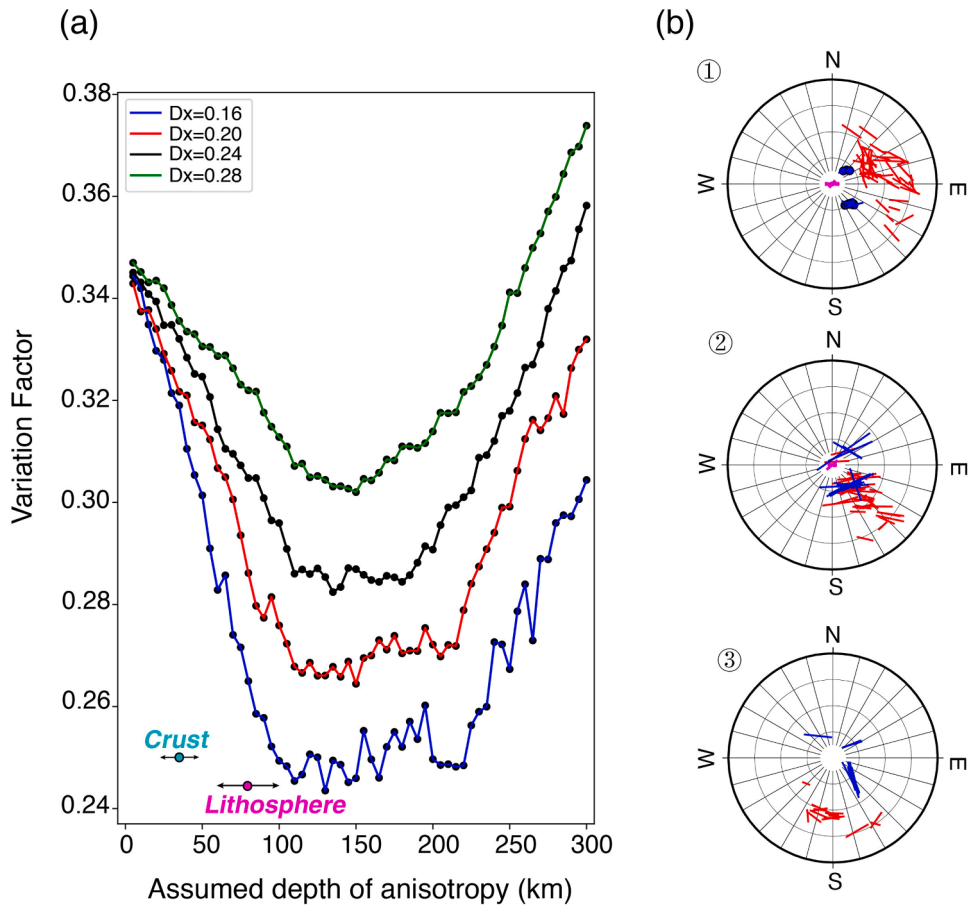

Fig. 6. (a) Results of spatial coherence analysis. Different colored lines represent results obtained with different grid sizes. (b) Same as Fig. 4(d) but for measurements projected to 150 km depth.

4.2. Localized upwelling and horizontal flow

In this study, the SKS splitting results are in good agreement with previous studies (Chen et al., 2017; Li et al., 2017; Lu et al., 2020; IRIS DMC, 2012; Fig. S7), showing distinctive differences between tectonic blocks. On a large scale across NE Asia, these studies have shown that the FPDs are generally perpendicular to the subduction slab contours, that is, a slight clockwise rotation from NWW-SEE trending FPDs in the North China Craton to NNW-SSE trending FPDs in the Jiamusi and northern Great Xing'an range. However, recent studies have revealed local deflections of FPDs as well as lateral variations in the splitting times between blocks (Li et al., 2017; Lu et al., 2020; Xu et al., 2023), thus suggesting localized upwelling and deflected radial spreading.

Around Changbaishan, most of the SKS phases with different back-azimuths show null results (Figs. 4(c) and 7). This result implies that LPO is either vertically aligned (e.g., due to dominant upward flow), or no significant LPO is present. However, local S measurements show significant shear wave splitting with scattered FPDs (Fig. 4(b)). In general, for a single-layer of horizontally aligned olivine, the measurements of SKS and local S should display similar FPDs, while the differences of splitting time are largely determined by the length of the ray-path in the anisotropic region. However, for the case of vertical or tilted anisotropy (e.g., caused by vertical flow), the differences in the splitting parameters of the two seismic phases can exhibit more complex characteristics, with an increase in delay time with increasing incidence angle and azimuthally dependent FPDs. In order to check how well the vertical flow hypothesis fits the observed data, we modeled the apparent splitting parameters generated by different fabrics of olivine (i.e., type-A, B, C, E; Jung et al., 2006) using the MSAT package (Walker and Wookey, 2012). Here we set a 100 km thick anisotropic layer centered at 150 km and simulated the apparent splitting parameters of the rays for given azimuths and incidence angles for a given rotation of the elastic moduli of olivine. We found that the predicted splitting parameters of near-vertical aligned type-E (Fig. 8) and type-A (Fig. S8) olivine match the pattern of the observations around the Changbaishan. Although the type-A fabric is the most general case in the upper mantle environment and provides a reasonable fit, the type-E fabric arguably can better fit both the observed FPDs and splitting times (Fig. S9). Such a fabric is usually developed in low-stress and moderate water content conditions, which is widely reported in the back-arc settings (e.g., Löberich et al., 2021). In any case, the combination of null measurements for sub-vertical teleseismic arrivals and higher splitting for events with higher incidence angles may point to a localized region of upwelling beneath the volcanic region, suggesting dominant vertical/near-vertical flow directly beneath Changbaishan. Recent surface-wave tomography results (Fan et al., 2021; Tang et al., 2022) are consistent with such assumption beneath Changbaishan, showing a near-vertical low-velocity body (−3 %) at 80–150 km depth that dips to the NE.

For the periphery of the volcanic region, the anisotropic depth inversion (Fig. 6) shows that in general, the local S and SKS splitting are most consistent at 125–175 km depth. Since this depth range is below the lithosphere-asthenosphere boundary (He et al., 2022; Zhang et al., 2022), our measured anisotropies represent horizontal mantle flow just below the base of the lithosphere. Laboratory experiments show that, for an upwelling beneath a slowly moving plate, azimuthal spreading of the plume head will cause concentrically aligned anisotropy (Druken et al., 2013). However, significant lateral variations in lithospheric thickness may alter the way in which an upwelling spread at its base, channeling

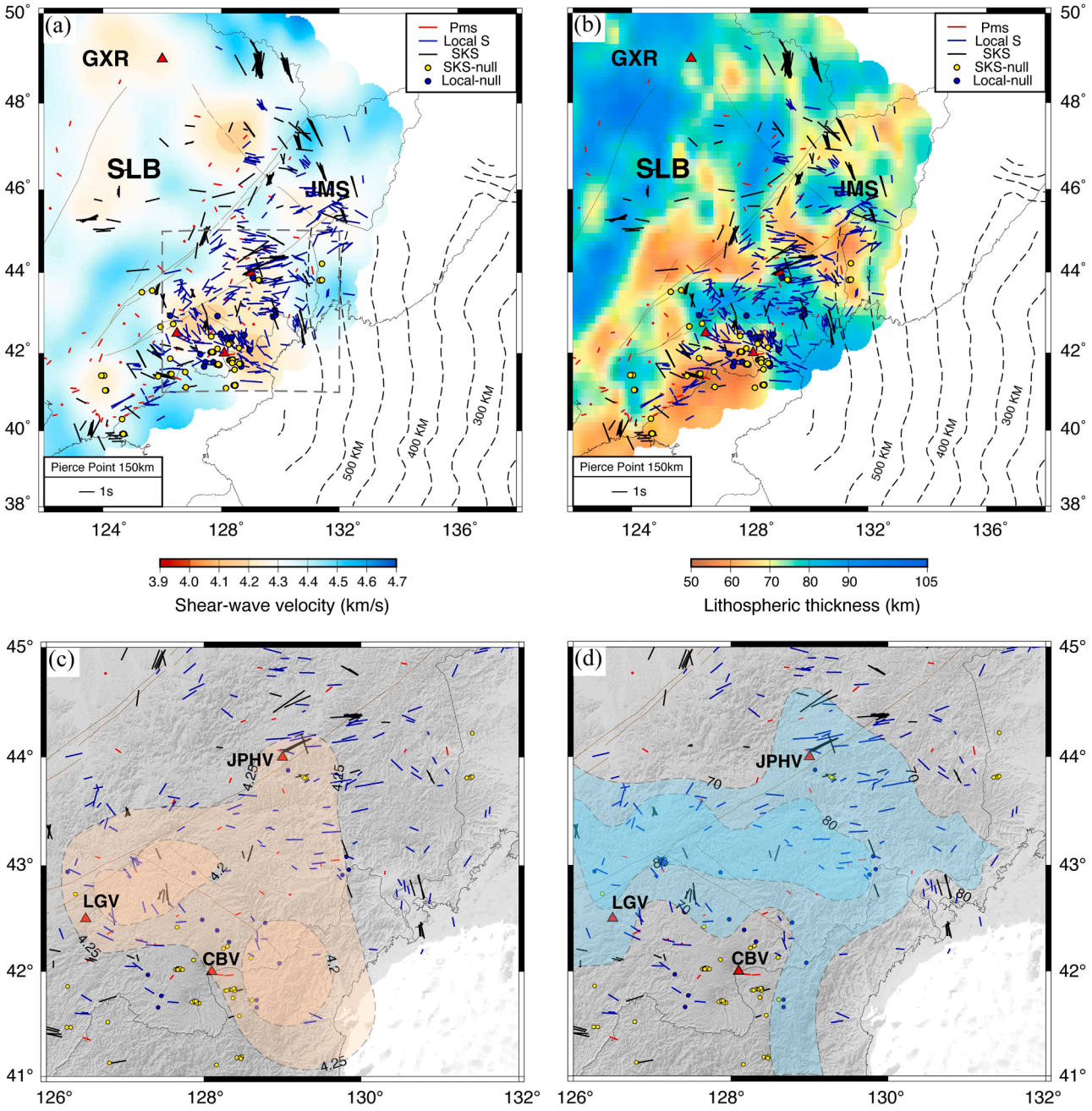

Fig. 7. Splitting measurements at a pierce point of 150 km. The trend and length of the short bars indicate the fast direction and strength of the anisotropy, with other details shown in the legend in the upper right of the figure. The contour plots represent the shear wave velocity (Fan et al., 2021) at 150 km (a) and regional lithospheric thickness model (b) from Zhang et al. (2022), respectively. (c) Zoomed-in view of the volcanic area. The orange shadow shows the 4.2 and 4.25 km/s velocity anomaly contours. (d) Same as (c) while the blue shadow shows the 70 and 80 km LAB contours. (For interpretation of the references to color in this figure legend, the reader is referred to the web version of this article.)

asthenospheric flow along gradients in lithospheric structure (Li et al., 2021). As upwelling is focused at the SW edge of a block of thicker lithosphere (Zhang et al., 2022), the plume is expected to spread asymmetrically, and preferentially to the SW. Such a flow pattern would explain the observed sub-concentric alignment of olivine around the periphery of the lithospheric block (Fig. 7). We suggest that upwelling beneath the volcanic region is channeled to the SW (towards Changbaishan). The thicker lithosphere above the low velocity body may represent a depleted residual of mantle melting, as proposed to exist beneath other intraplate volcanoes (Lodge and Helffrich, 2006; Rychert et al., 2013). This restite root may originate from a longer history of magmatism in the study area, preferentially deflecting the main upwelling towards the SW (Fig. 9).

4.3. Explanation for deep origin

Understanding mantle flow in the asthenosphere can help to clarify the origin of the NE China Holocene intraplate volcanoes. In this region, large-scale upwelling return flow in the BMW is often invoked to explain intraplate volcanism, which would then be sustained by active dehydration of the slab (Zhao et al., 2012), entrainment of a hydrous mantle from the MTZ (Yang and Faccenda, 2020), or small-scale convection (Long et al., 2019). In the framework of the BMW, all of these models predict mantle flow in the back-arc region to be trench-perpendicular,

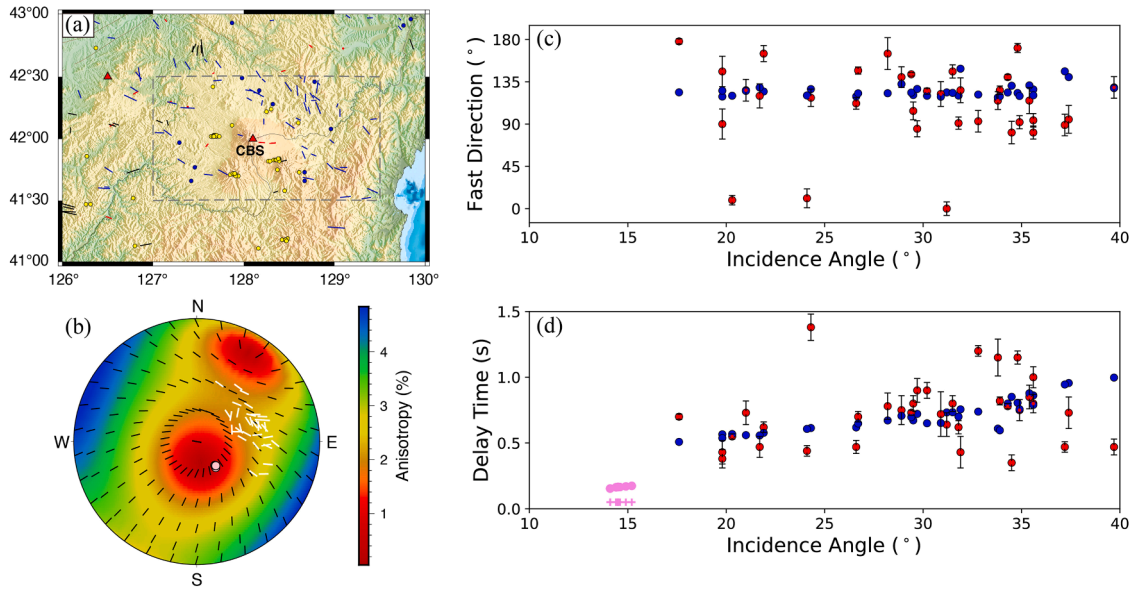

Fig. 8. (a) Splitting results for the Changbaishan region with gray box indicating the location used for forward-modeling. We refrain from showing the higher incidence angle FPDs for local S waves in Fig. 7c and d to better highlight the flow patterns, with null measurements showing vertical flow and FPD showing horizontal alignments. (b) Lower hemispherical projection for E-type olivine, with 65 % alignment of crystals. Olivine is rotated with $\alpha = 75°$, $\beta = 65°$, $\gamma = 45°$ around 1-, 2-, 3-axes, respectively and where $\beta = 90°$ would show vertical flow. Black ticks show expected FPD and white bars show the data. Pink circles denote the null results of SKS measurements. Note that here we use the actual event locations from each splitting measurement and estimate the incidence angle at a depth of 150 km using the IASP91 velocity model. (c, d) FPD and delay times as a function of incidence angle. Red circles show data and blue circles show the expected results for the same azimuth and incidence angle for the elastic constants in (b). null measurements are denoted by a pink cross with a delay time of 0 s. Predicted delay times are indicated by pink circles. (For interpretation of the references to color in this figure legend, the reader is referred to the web version of this article.)

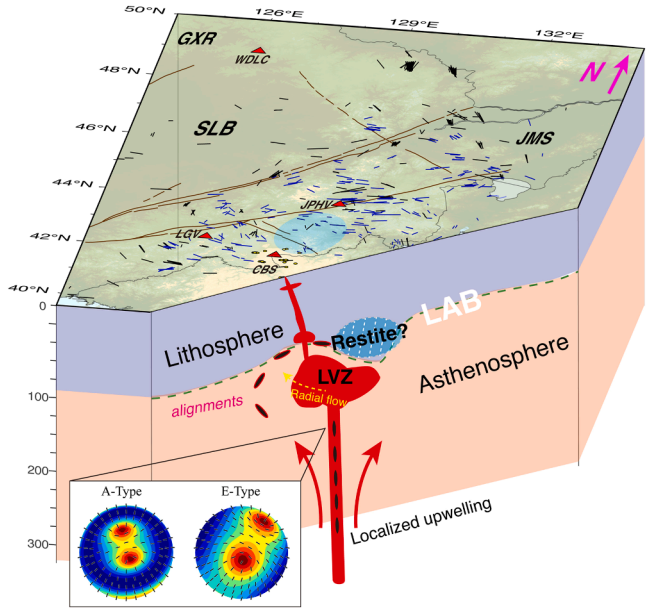

Fig. 9. A cartoon diagram showing a localized upwelling beneath Changbaishan.

accompanied by slight variations due to slab morphology, and with a broad mantle upwelling in response to corner flow. Such interpretation does indeed explain the first-order trench-perpendicular FPDs seen in the SKS splitting from the North China Craton to the northern Great Xing'an range (Li et al., 2017; IRIS DMC, 2012). However, none of these models predict localized upwelling close to the slab "hinge" near Changbaishan, where the slab just arrives in the MTZ and starts to flatten. Furthermore, our findings of more trench parallel FPDs at the periphery of localized upwelling is also inconsistent with that expected for large-scale flow in the BMW or edge driven convection (Manjón-Cabeza Córdoba and Ballmer, 2021).

Therefore, an anomalous feature of the deeper mantle must drive such a localized mantle upwelling. Magnetotelluric (MT) imaging has revealed significant low-resistivity anomalies extending upward from the MTZ to the base of lithosphere beneath Changbaishan through narrow channels (Li et al., 2020). Moreover, the Sr-Nd-Pb-Hf isotopic compositions of the Changbaishan and Longgang sodic basalts differ from those of other potassic volcanoes located above the stagnant slab front, thus may not prefer the contribution of recycled ancient sediments and water carried by the subducted Pacific plate to melting as well (Xu et al., 2021). The exact origin of the upwelling is beyond the scope of this study as it requires more detailed imaging of the MTZ and/or lower mantle, but localized upwelling through a slab gap or tear (Kim et al., 2021; Tang et al., 2014) is a viable candidate. As the Pacific slab rolls back toward the east, dynamic overpressures may inject hot and/or hydrous materials from the sub-Pacific mantle (Morishige et al., 2010) through a slab gap/tear and into the BMW locally to sustain Changbaishan volcanism. Alternatively, the subduction slab beneath Changbaishan may be anomalous in some way driving localized upwelling in this region. Future seismic studies exploiting dense deployments in NE China and the DPRK will help to further constrain this.

5. Conclusion

In this study, we analyse the splitting parameters of three seismic phases in NE China to reveal the genesis and dynamics of intraplate volcanism in the region. We show that, the inclusion of local S splitting across a wide depth range, and thus also a wide range of incidence angles, can significantly improve the constraints on arbitrary axial anisotropy and lateral variability allowing vertical mantle flow to be constrained from shear wave splitting data. The combination of circular anisotropic patterns in the region enclosed by the Changbaishan, Longgang and Jingpohu volcanoes, driven by divergent flow at the base of the lithosphere, together with many "null" results directly beneath

Changbaishan and local splitting consistent with sub-vertical flow, provide strong evidence for a localized mantle upwelling beneath Changbaishan. We suggest this is best explained by upwelling through an anomalous region of the subducting slab beneath the volcano, such as through a slab gap or tear. At shallow depth, the upwelling appears to be deflected to the SW, possibly controlled by topography at the base of the lithosphere.

CRediT authorship contribution statement

Cunrui Han: Writing – review & editing, Writing – original draft, Software, Methodology, Formal analysis. **James O.S. Hammond:** Conceptualization, Formal analysis, Supervision, Validation, Writing – review & editing. **Maxim D. Ballmer:** Formal analysis, Validation, Writing – review & editing. **Wei Wei:** Validation, Formal analysis. **Mijian Xu:** Writing – review & editing, Formal analysis. **Zhouchuan Huang:** Software, Formal analysis. **Liangshu Wang:** Data curation.

Declaration of Competing Interest

The authors declare that they have no known competing financial interests or personal relationships that could have appeared to influence the work reported in this paper.

Data availability

Data will be made available on request.

Acknowledgement

We thank the US Government and the Richard Lounsbery Foundation for funding to support the activities of the Mount Paektu Research Centre (MPRC) and support for C.H. and J.O.S.H. J.O.S.H is also supported by a NERC Knowledge Exchange Fellowship (NE/X001717/1). All seismic data from DPRK and NE China are available at IRIS Data Management Center and the Data Management Centre of China National Seismic Network (http://www.seisdmc.ac.cn). We are grateful to Editor Prof. Hans Thybo, Prof. Vadim Levin and an anonymous referee for their constructive reviews that significantly improve this manuscript. We thank James Wookey and Andrew Walker for providing the MSAT code (https://www1.gly.bris.ac.uk/MSAT/). C. H. is also grateful to Yajing Bi, Jing Shi, and Li Wang for their fruitful discussions. Most figures were created by GMT (Wessel et al., 2013).

Supplementary materials

Supplementary material associated with this article can be found, in the online version, at doi:10.1016/j.epsl.2023.118495.

References

Ai, Y., He, Y., 2007. *NCISP6*. International Federation of Digital Seismograph Networks. doi:10.7914/SN/1A_2007.

Bi, Y., Huang, Z., Wang, H., Wu, H., 2020. Upper-mantle anisotropy and dynamics beneath Northeast Asia: insight from SKS and local S splitting analysis. Geochem. Geophys. Geosyst. 21 (8) https://doi.org/10.1029/2020GC009160 e2020GC009160.

Bianchi, I., Pezzo, G., Giordano, G., Chiarabba, C., 2023. Progressive underplating of mafic material at mid-crustal depth beneath Ischia volcano, Italy. Commun. Earth Environ. 4 (1), 303. https://doi.org/10.1038/s43247-023-00938-8.

Bowman, J.R., Ando, M., 1987. Shear-wave splitting in the upper-mantle wedge above the Tonga subduction zone. Geophys. J. Int. 88 (1), 25–41. https://doi.org/10.1111/j.1365-246X.1987.tb01367.x.

Chen, H., Niu, F., Obayashi, M., Grand, S.P., Kawakatsu, H., Chen, Y.J., Ning, J., Tanaka, S., 2017. Mantle seismic anisotropy beneath NE China and implications for the lithospheric delamination hypothesis beneath the southern Great Xing'an range. Earth Planet. Sci. Lett. 471, 32–41. https://doi.org/10.1016/j.epsl.2017.04.030.

Chun, K.-Y., Richards, P.G., 2004. Dongbei Broadband Network [Data set]. International Federation of Digital Seismograph Networks. doi:10.7914/SN/5G_2004.

Crampin, S., 1984. Effective anisotropic elastic constants for wave propagation through cracked solids. Geophys. J. Int. v. 76 (1), 135–145. https://doi.org/10.1111/j.1365-246X.1984.tb05029.x.

Druken, K.A., Kincaid, C., Griffiths, R.W., 2013. Directions of seismic anisotropy in laboratory models of mantle plumes. Geophys. Res. Lett. 40 (14), 3544–3549. https://doi.org/10.1002/grl.50671.

Fan, X., Chen, Q.F., Ai, Y., Chen, L., Jiang, M., Wu, Q., Guo, Z., 2021. Quaternary sodic and potassic intraplate volcanism in northeast China controlled by the underlying heterogeneous lithospheric structures. Geology 49 (10), 1260–1264. https://doi.org/10.1130/G48932.1.

Fan, X., Chen, Q.F., Legendre, C.P., Guo, Z., 2020. Intraplate volcanism and regional geodynamics in NE Asia revealed by anisotropic Rayleigh-wave tomography. Geophys. Res. Lett. 47 (1) https://doi.org/10.1029/2019GL085623 e2019GL085623.

Grand, S., Ni, J., 2009. Collaborative Research: northeast China Extended Seismic Array: deep subduction, mantle dynamics and lithospheric evolution beneath Northeast China [Data set]. International Federation of Digital Seismograph Networks. doi:10.7914/SN/YP_2009.

Hammond, J.O.S., 2014. Constraining melt geometries beneath the Afar Depression, Ethiopia from teleseismic receiver functions: the anisotropic H-κ stacking technique. Geochem. Geophys. Geosyst. 15 (4), 1316–1332. https://doi.org/10.1002/2013GC005186.

Hammond, J.O.S., Wu, J.P., Ri, K.S., Wei, W., Yu, J.N., Oppenheimer, C., 2020. Distribution of partial melt beneath Changbaishan/Paektu volcano, China/Democratic people's Republic of Korea. Geochem. Geophys. Geosyst. 21 (1) https://doi.org/10.1029/2019GC008461 e2019GC008461.

Han, C., Xu, M., Huang, Z., Wang, L., Xu, M., Mi, N., Yu, D., Gou, T., Wang, H., Hao, S., Tian, M., Bi, Y., 2020. Layered crustal anisotropy and deformation in the SE Tibetan plateau revealed by Markov–Chain–Monte–Carlo inversion of receiver functions. Phys. Earth Planet. Inter. 306, 106522 https://doi.org/10.1016/j.pepi.2020.106522.

He, Y., Chen, Q.F., Chen, L., Wang, X., Guo, G., Li, T., Zhang, K., Li, J., Chen, Y., 2022. Distinct lithospheric structure in the Xing'an-Mongolian orogenic belt. Geophys. Res. Lett. 49 (10) https://doi.org/10.1029/2021GL097283 e2021GL097283.

Hayes, G., 2018. Slab2 - A Comprehensive Subduction Zone Geometry Model: U.S. Geological Survey data release, doi:10.5066/F7PV6JNV.

IRIS DMC, 2012. Data Services Products: SWS-DBs Shear-wave splitting databases. doi:10.17611/DP/SWS.1.

Jung, H., Katayama, I., Jiang, Z., Hiraga, T., Karato, S.I., 2006. Effect of water and stress on the lattice-preferred orientation of olivine. Tectonophysics 421 (1–2), 1–22. https://doi.org/10.1016/j.tecto.2006.02.011.

Kim, Y.W., Chang, S.J., Witek, M., Ning, J., Wen, J., 2021. S-velocity mantle structure of East Asia from teleseismic traveltime tomography: inferred mechanisms for the Cenozoic intraplate volcanoes. J. Geophys. Res., Solid Earth 126 (3). https://doi.org/10.1029/2020JB020345 e2020JB020345.

Levin, V., Long, M.D., Skryzalin, P., Li, Y., López, I., 2018. Seismic evidence for a recently formed mantle upwelling beneath New England. Geology 46 (1), 87–90. https://doi.org/10.1130/G39641.1.

Li, S., Guo, Z., Chen, Y.J., 2017. Complicated 3D mantle flow beneath Northeast China from shear wave splitting and its implication for the Cenozoic intraplate volcanism. Tectonophysics 709, 1–8. https://doi.org/10.1016/j.tecto.2017.04.015.

Li, S.W., Weng, A.H., Li, J.P., Shan, X.L., Han, J.T., Tang, Y., Zhang, Y.H., Wang, X.Q., 2020. The deep origins of Cenozoic volcanoes in Northeast China revealed by 3-D electrical structure. Sci. China 63, 533–547. https://doi.org/10.1007/s11430-018-9537-2.

Li, Y., Weng, A., Xu, W., Zou, Z., Tang, Y., Zhou, Z., Li, S., Zhang, Y., Ventura, G., 2021. Translithospheric magma plumbing system of intraplate volcanoes as revealed by electrical resistivity imaging. Geology 49 (11), 1337–1342. https://doi.org/10.1130/G49032.1.

Liu, H., Niu, F., 2012. Estimating crustal seismic anisotropy with a joint analysis of radial and transverse receiver function data. Geophys. J. Int. 188 (1), 144–164. https://doi.org/10.1111/j.1365-246X.2011.05249.x.

Liu, J., Han, J., Fyfe, W.S., 2001. Cenozoic episodic volcanism and continental rifting in northeast China and possible link to Japan Sea development as revealed from K–Ar geochronology. Tectonophysics 339 (3–4), 385–401. https://doi.org/10.1016/S0040-1951(01)00132-9.

Liu, K.H., Gao, S.S., Gao, Y., Wu, J., 2008. Shear wave splitting and mantle flow associated with the deflected Pacific slab beneath northeast Asia. J. Geophys. Res., Solid Earth 113, B01305. https://doi.org/10.1029/2007JB005178.

Liu, K.H., Gao, S.S., 2011. Estimation of the depth of anisotropy using spatial coherency of shear-wave splitting parameters. Bull. Seismol. Soc. Am. 101 (5), 2153–2161. https://doi.org/10.1785/0120100258.

Löberich, E., Long, M.D., Wagner, L.S., Qorbani, E., Bokelmann, G., 2021. Constraints on olivine deformation from SKS shear-wave splitting beneath the southern Cascadia subduction zone Back-Arc. Geochem. Geophys. Geosyst. 22 (11) https://doi.org/10.1029/2021GC010091 e2021GC010091.

Lodge, A., Helffrich, G., 2006. Depleted swell root beneath the Cape Verde Islands. Geology 34 (6), 449–452. https://doi.org/10.1130/G22030.1.

Long, X., Ballmer, M.D., Córdoba, A.M.C., Li, C.F., 2019. Mantle melting and intraplate volcanism due to self-buoyant hydrous upwellings from the stagnant slab that are conveyed by small-scale convection. Geochem. Geophys. Geosyst. 20 (11), 4972–4997. https://doi.org/10.1029/2019GC008591.

Lu, M., Lei, J., Zhao, D., Ai, Y., Xu, X., Zhang, G., 2020. SKS splitting measurements in NE China: new insights into the Wudalianchi intraplate volcanism and mantle dynamics. J. Geophys. Res., Solid Earth 125 (3). https://doi.org/10.1029/2019JB018575 e2019JB018575.

Mainprice, D., 2007. Seismic anisotropy of the deep Earth from a mineral and rock physics perspective. In: Schubert, G. (Ed.), Treatise on Geophysics. Elsevier Ltd., Oxford, pp. 437–491.
Manjón-Cabeza Córdoba, A., Ballmer, M.D., 2021. The role of edge-driven convection in the generation of volcanism—Part 1: a 2D systematic study. Solid Earth 12 (3), 613–632. https://doi.org/10.5194/se-12-613-2021.
Morishige, M., Honda, S., Yoshida, M., 2010. Possibility of hot anomaly in the sub-slab mantle as an origin of low seismic velocity anomaly under the subducting Pacific plate. Phys. Earth Planet. Inter. 183 (1–2), 353–365. https://doi.org/10.1016/j.pepi.2010.04.002.
Mount Paektu Research Centre, 2013. https://doi.org/10.7914/SN/1U.
Niu, F., Li, J., 2011. Component azimuths of the CEArray stations estimated from P-wave particle motion. Earthq. Sci. 24 (1), 3–13. https://doi.org/10.1007/s11589-011-0764-8.
Oppenheimer, C., Wacker, L., Xu, J., Galván, J.D., Stoffel, M., Guillet, S., Corona, C., Sigl, M., Cosmo, N.D., Hajdas, I., Pan, B., Breuker, R., Schneider, L., Esper, J., Fei, J., Hammond, J.O.S., Büntgen, U., 2017. Multi-proxy dating the 'Millennium Eruption' of Changbaishan to late 946 CE. Quat. Sci. Rev. 158, 164–171. https://doi.org/10.1016/j.quascirev.2016.12.024.
Park, J., Chen, X., Levin, V., 2023. Crustal anisotropy from the birefringence of P-to-S converted waves: bias associated with P-wave anisotropy. Ann. Geophys. 66 (2), SE205. https://doi.org/10.4401/ag-8882.
Paulssen, H., 2004. Crustal anisotropy in southern California from local earthquake data. Geophys. Res. Lett. 31 (1), L01601. https://doi.org/10.1029/2003GL018654.
Rychert, C.A., Laske, G., Harmon, N., Shearer, P.M., 2013. Seismic imaging of melt in a displaced Hawaiian plume. Nat. Geosci. 6 (8), 657–660. https://doi.org/10.1038/ngeo1878.
Salimbeni, S., Pondrelli, S., Margheriti, L., Park, J., Levin, V., 2008. SKS splitting measurements beneath Northern Apennines region: a case of oblique trench-retreat. Tectonophysics 462 (1–4), 68–82. https://doi.org/10.1016/j.tecto.2007.11.075.
Silver, P.G., Chan, W.W., 1991. Shear wave splitting and subcontinental mantle deformation. J. Geophys. Res., Solid Earth 96 (B10), 16429–16454. https://doi.org/10.1029/91JB00899.
Tang, Y., Obayashi, M., Niu, F., Grand, S.P., Chen, Y.J., Kawakatsu, H., Tanaka, S., Ning, J., Ni, J.F., 2014. Changbaishan volcanism in northeast China linked to subduction-induced mantle upwelling. Nat. Geosci. 7 (6), 470–475. https://doi.org/10.1038/ngeo2166.
Tang, Z., Julià, J., Mai, P.M., Mooney, W.D., Wu, Y., 2022. Shear-wave velocity structure beneath Northeast China from joint inversion of receiver functions and Rayleigh wave phase velocities: implications for intraplate volcanism. J. Geophys. Res., Solid Earth 127 (5). https://doi.org/10.1029/2022JB023956 e2022JB023956.
Tao, K., Niu, F., Ning, J., Chen, Y.J., Grand, S., Kawakatsu, H., Tanaka, S., Obayashi, M., Ni, J., 2014. Crustal structure beneath NE China imaged by NECESSArray receiver function data. Earth Planet. Sci. Lett. 398, 48–57. https://doi.org/10.1016/j.epsl.2014.04.043.
Tao, K., Grand, S.P., Niu, F., 2018. Seismic structure of the upper mantle beneath eastern Asia from full waveform seismic tomography. Geochem. Geophys. Geosyst. 19 (8), 2732–2763. https://doi.org/10.1029/2018GC007460.
Teanby, N.A., Kendall, J.M., Van der Baan, M., 2004. Automation of shear-wave splitting measurements using cluster analysis. Bull. Seismol. Soc. Am. 94 (2), 453–463. https://doi.org/10.1785/0120030123.
Tian, Z.Y., Han, P., Xu, K.D., 1992. The Mesozoic-Cenozoic East China rift system. Tectonophysics 208 (1–3), 341–363. https://doi.org/10.1016/0040-1951(92)90354-9.
Vinnik, L.P., Kosarev, G.L., Makeyeva, L.I., 1984. Anisotropy of the lithosphere from the observations of SKS and SKKS. Proc. Acad. Sci. USSR 278, 1335–1339 (In Russia).
Walker, A.M., Wookey, J., 2012. MSAT—A new toolkit for the analysis of elastic and seismic anisotropy. Comput. Geosci. 49, 81–90. https://doi.org/10.1016/j.cageo.2012.05.031.
Walsh, E., Arnold, R., Savage, M.K., 2013. Silver and Chan revisited. J. Geophys. Res., Solid Earth 118 (10), 5500–5515. https://doi.org/10.1002/jgrb.50386.
Wang, X.J., Chen, L.H., Hofmann, A.W., Mao, F.G., Liu, J.Q., Zhong, Y., Xie, L.W., Yang, Y.H., 2017. Mantle transition zone-derived EM1 component beneath NE China: geochemical evidence from Cenozoic potassic basalts. Earth Planet. Sci. Lett. 465, 16–28. https://doi.org/10.1016/j.epsl.2017.02.028.
Ward, J.F., Rosenbaum, G., Ubide, T., Wu, J., Caulfield, J.T., Sandiford, M., Gürer, D., 2021. Geophysical and geochemical constraints on the origin of Holocene intraplate volcanism in East Asia. Earth-Science Rev. 218, 103624 https://doi.org/10.1016/j.earscirev.2021.103624.
Wei, W., Hammond, J.O.S., Zhao, D., Xu, J., Liu, Q., Gu, Y., 2019. Seismic evidence for a mantle transition zone origin of the Wudalianchi and Halaha volcanoes in northeast China. Geochem. Geophys. Geosyst. 20 (1), 398–416. https://doi.org/10.1029/2018GC007663.
Wessel, P., Smith, W.H., Scharroo, R., Luis, J., Wobbe, F., 2013. Generic mapping tools: improved version released. Eos Trans. AGU 94 (45), 409–410. https://doi.org/10.1002/2013EO450001.
Wilde, S.A., 2015. Final amalgamation of the Central Asian Orogenic Belt in NE China: Paleo-Asian Ocean closure versus Paleo-Pacific plate subduction—A review of the evidence. Tectonophysics 662, 345–362. https://doi.org/10.1016/j.tecto.2015.05.006.
Wüstefeld, A., Bokelmann, G., Barruol, G., 2010. Evidence for ancient lithospheric deformation in the East European Craton based on mantle seismic anisotropy and crustal magnetics. Tectonophysics 481 (1–4), 16–28. https://doi.org/10.1016/j.tecto.2009.01.010.
Xu, J., Liu, G., Wu, J., Ming, Y., Wang, Q., Cui, D., Shangguan, Z., Pan, B., Lin, X., Liu, J., 2012. Recent unrest of Changbaishan volcano, northeast China: a precursor of a future eruption? Geophys. Res. Lett. 39 (16), L16305. https://doi.org/10.1029/2012GL052600.
Xu, M., Huang, Z., Wang, L., Xu, M., Zhang, Y., Mi, N., Yu, D., Yuan, X., 2020. Sharp lateral Moho variations across the SE Tibetan margin and their implications for plateau growth. J. Geophys. Res., Solid Earth 125 (5). https://doi.org/10.1029/2019JB018117 e2019JB018117.
Xu, T., Ai, Y., Wu, C., Chen, L., Fan, E., Li, L., Dong, W., 2023. Subduction-induced asthenospheric flow around the Songliao Basin in NE China revealed by shear wave splitting measurements of dense seismic arrays. J. Geophys. Res., Solid Earth. https://doi.org/10.1029/2022JB026075 e2022JB026075.
Xu, M., Li, Y., Hou, H., Wang, C., Gao, R., Wang, H., Han, Z., Zhou, A., 2017. Structural characteristics of the Yilan–Yitong and Dunhua–Mishan faults as northern extensions of the Tancheng–Lujiang Fault Zone: new deep seismic reflection results. Tectonophysics 706, 35–45. https://doi.org/10.1016/j.tecto.2017.03.018.
Xu, W.L., Chen, J.H., Weng, A.H., Tang, J., Wang, F., Wang, C.G., Guo, P., Wang, Y.N., Yang, H., Sorokin, A.A., 2021. Stagnant slab front within the mantle transition zone controls the formation of Cenozoic intracontinental high-Mg andesites in northeast Asia. Geology 49 (1), 19–24. https://doi.org/10.1130/G47917.1.
Yang, J., Faccenda, M., 2020. Intraplate volcanism originating from upwelling hydrous mantle transition zone. Nature 579 (7797), 88–91. https://doi.org/10.1038/s41586-020-2045-y.
Zhang, A., Guo, Z., Afonso, J.C., Handley, H., Dai, H., Yang, Y., Chen, Y.J., 2022. Lithosphere–asthenosphere interactions beneath northeast China and the origin of its intraplate volcanism. Geology 50 (2), 210–215. https://doi.org/10.1130/G49375.1.
Zhang, R., Wu, Q., Sun, L., He, J., Gao, Z., 2014. Crustal and lithospheric structure of Northeast China from S-wave receiver functions. Earth Planet. Sci. Lett. 401, 196–205. https://doi.org/10.1016/j.epsl.2014.06.017.
Zhao, D., Yanada, T., Hasegawa, A., Umino, N., Wei, W., 2012. Imaging the subducting slabs and mantle upwelling under the Japan Islands. Geophys. J. Int. 190 (2), 816–828. https://doi.org/10.1111/j.1365-246X.2012.05550.x.